



# Empirical methods for the estimation of Southern Ocean CO<sub>2</sub>: support vector and random forest regression

Luke Gregor<sup>1,2</sup>, Schalk Kok<sup>3</sup>, and Pedro M. S. Monteiro<sup>1</sup>

<sup>1</sup>Southern Ocean Carbon-Climate Observatory (SOCCO), CSIR, Cape Town, South Africa

<sup>2</sup>University of Cape Town, Department of Oceanography, Cape Town, South Africa

<sup>3</sup>University of Pretoria, Department of Mechanical and Aeronautical Engineering, Pretoria, South Africa

Correspondence to: Luke Gregor (luke.gregor@uct.ac.za)

Received: 29 May 2017 – Discussion started: 12 June 2017

Revised: 3 October 2017 – Accepted: 5 November 2017 – Published: 8 December 2017

**Abstract.** The Southern Ocean accounts for 40 % of oceanic CO<sub>2</sub> uptake, but the estimates are bound by large uncertainties due to a paucity in observations. Gap-filling empirical methods have been used to good effect to approximate  $p\text{CO}_2$  from satellite observable variables in other parts of the ocean, but many of these methods are not in agreement in the Southern Ocean. In this study we propose two additional methods that perform well in the Southern Ocean: support vector regression (SVR) and random forest regression (RFR). The methods are used to estimate  $\Delta p\text{CO}_2$  in the Southern Ocean based on SOCAT v3, achieving similar trends to the SOM-FFN method by Landschützer et al. (2014). Results show that the SOM-FFN and RFR approaches have RMSEs of similar magnitude (14.84 and 16.45  $\mu\text{atm}$ , where 1 atm = 101 325 Pa) where the SVR method has a larger RMSE (24.40  $\mu\text{atm}$ ). However, the larger errors for SVR and RFR are, in part, due to an increase in coastal observations from SOCAT v2 to v3, where the SOM-FFN method used v2 data. The success of both SOM-FFN and RFR depends on the ability to adapt to different modes of variability. The SOM-FFN achieves this by having independent regression models for each cluster, while this flexibility is intrinsic to the RFR method. Analyses of the estimates shows that the SVR and RFR's respective sensitivity and robustness to outliers define the outcome significantly. Further analyses on the methods were performed by using a synthetic dataset to assess the following: which method (RFR or SVR) has the best performance? What is the effect of using time, latitude and longitude as proxy variables on  $\Delta p\text{CO}_2$ ? What is the impact of the sampling bias in the SOCAT v3 dataset on the estimates? We find that while RFR is indeed better than SVR,

the ensemble of the two methods outperforms either one, due to complementary strengths and weaknesses of the methods. Results also show that for the RFR and SVR implementations, it is better to include coordinates as proxy variables as RMSE scores are lowered and the phasing of the seasonal cycle is more accurate. Lastly, we show that there is only a weak bias due to undersampling. The synthetic data provide a useful framework to test methods in regions of sparse data coverage and show potential as a useful tool to evaluate methods in future studies.

## 1 Introduction

The global oceans have played an important role in mitigating the effects of climate change by taking up 25 % of anthropogenic CO<sub>2</sub> emissions annually (Khaliwala et al., 2013; Le Quéré et al., 2016). The Southern Ocean has played a disproportionate role in this uptake, accounting for 40 % of the oceanic anthropogenic CO<sub>2</sub> uptake (Khaliwala et al., 2013; Frölicher et al., 2015). Yet, despite the region's importance, first-order CO<sub>2</sub> flux estimates are bound by large uncertainties due to sparse observations in the Southern Ocean (Lenton et al., 2006; Monteiro, 2010; Lenton et al., 2012; Takahashi et al., 2012; Bakker et al., 2016). These uncertainties limit our capacity to resolve variability and trends of CO<sub>2</sub>.

Viable alternative methods to estimate net CO<sub>2</sub> flux are atmospheric CO<sub>2</sub> inversions, ocean biogeochemical process models and empirical models (Rödenbeck et al., 2015). As shown by Le Quéré et al. (2007), atmospheric CO<sub>2</sub> inversions are useful tools to estimate the net CO<sub>2</sub> fluxes, but fail to

offer further understanding with spatially integrated air–sea flux estimates (Fay and McKinley, 2014). Conversely, ocean biogeochemical process models are good tools for mechanistic understanding, but fail to represent the seasonality of CO<sub>2</sub> fluxes in the Southern Ocean (Lenton et al., 2013; Mongwe et al., 2016). Empirical modelling offers an opportunity to bridge the gap between sparse data in the Southern Ocean and correct parameterization of future earth system models.

Empirical models maximize the utility of existing surface ocean CO<sub>2</sub> observations ( $p\text{CO}_2$ ) by interpolating these with satellite proxy data. Access to in situ  $p\text{CO}_2$  data, via platforms such as SOCAT (Surface Ocean CO<sub>2</sub> Atlas), has been crucial to the success of empirical methods (Rödenbeck et al., 2015; Bakker et al., 2016). This, in conjunction with the increasing use of machine learning, has seen a proliferation in the number and diversity of methods in the literature. Rödenbeck et al. (2015) compared a suite of 14 methods using a regional framework provided by Fay and McKinley (2014). The majority of these methods are variants of multiple linear regression (MLR) or artificial neural networks (ANNs), with regression being applied in regional windows or clusters based on climatologies of satellite measurable variables. The authors found that methods agreed in regions where data coverage was adequate, but for data-sparse regions, such as the Southern Ocean, the interannual CO<sub>2</sub> variability of various empirical methods was not coherent.

Only two of the methods in Rödenbeck et al. (2015) were able to adequately represent interannual variability of  $\Delta p\text{CO}_2$ , namely: the SOM-FFN (self-organizing map–feed-forward neural network) from Landschützer et al. (2014), and the mixed layer scheme (MLS) from Rödenbeck et al. (2014). These two methods were used by Landschützer et al. (2015) to show that Southern Ocean CO<sub>2</sub> uptake strengthened after 2000. However, these methods often showed large interannual differences in flux estimates despite agreeing on the overall decadal trend. This shows that there is lack of coherence even amongst the methods that perform well, meaning that different methods may lead to different interpretation of the drivers of  $\Delta p\text{CO}_2$ . The primary reason for the varied results is thought to be the way in which the algorithms deal with sparse data in the Southern Ocean (Rödenbeck et al., 2015). This alludes to the importance of testing multiple approaches, as different methods may be able to better represent the CO<sub>2</sub> estimates in the data-sparse Southern Ocean.

In this study we introduce two methods new to this application, namely: support vector regression (SVR) and random forest regression (RFR). SVR is a method based on the theory of statistical learning, making the method robust to overfitting by statistically determining the complexity of a problem rather than a heuristic approach as required in setting up an ANNs hidden layer structure (Vapnik, 1999; Smola et al., 2004). In a review on the use of support vector machines (the broad category for regression and classification variants) in remote sensing, Mountrakis et al. (2011) found that the

method had the “ability to generalize well even with limited training samples”. This makes SVR an appealing consideration for the sparsely sampled Southern Ocean. RFR uses an ensemble of decision trees to create robust estimates, often without requiring data pre-processing, making it an effective “off the shelf” method (Louppe, 2014). As with SVM, random forests (both classification and regression variants) have also been used in remote sensing applications, though it does not seem to be as widely used in earth system sciences despite proving to be a powerful, yet easy to implement, learning algorithm (Caruana and Niculescu-Mizil, 2006; Hastie et al., 2009). We use SVR and RFR to estimate CO<sub>2</sub> fluxes in the Southern Ocean to try to better resolve the seasonal cycle from 1998 to 2014. These methods are trained with SOCAT v3 data collocated with satellite proxies. We compare these results with those of Landschützer et al. (2014). However, the lack of data in the Southern Ocean, particularly in winter, makes it difficult to understand the limitations of these methods within the context of SOCAT data.

To gain a better understanding of these methods’ strengths and weaknesses we implement SVR and RFR in a synthetic data environment. A similar approach was taken by Friedrich and Oeschies (2009) in the North Atlantic, which experienced a similar data paucity to the Southern Ocean in the early 2000s. This idealized environment was also used to estimate the effect of including or excluding certain proxy variables as well as the optimal coverage of cruise tracks to constrain the North Atlantic  $\Delta p\text{CO}_2$  adequately. Similarly, we assess the efficacy of including coordinate variables as proxies of  $\Delta p\text{CO}_2$  in the empirical methods. In the inter-comparison study by Rödenbeck et al. (2015) proxies typically include, but are not limited to, sea surface temperature (SST), chlorophyll *a* (Chl *a*), mixed layer depth (MLD) and sea surface salinity (SSS); however, several methods in the study also include latitude and longitude. While coordinates do not mechanistically impact  $\Delta p\text{CO}_2$ , they do help to constrain estimates where the available remote sensing proxies cannot adequately do so. The synthetic data are also used to test the ability of the SVR and RFR to approximate  $\Delta p\text{CO}_2$  in the seasonally sparse Southern Ocean.

## 2 Data and methods

This study is presented in two parts. The first applies SVR and RFR to the SOCAT v3 dataset and compares these outputs with those of the SOM-FFN by Landschützer et al. (2014). These estimates will be referred to as the observational estimates. Here the domain is limited to the three Southern Ocean domains of Fay and McKinley (2014) that are shown in Fig. 1. These biomes are used to assess the performance of each of the methods, as done in Rödenbeck et al. (2015). Fay and McKinley (2014) use a different nomenclature, which roughly corresponds to frontal zones. We rename the sub-tropical seasonally stratified biome (STSS) as the

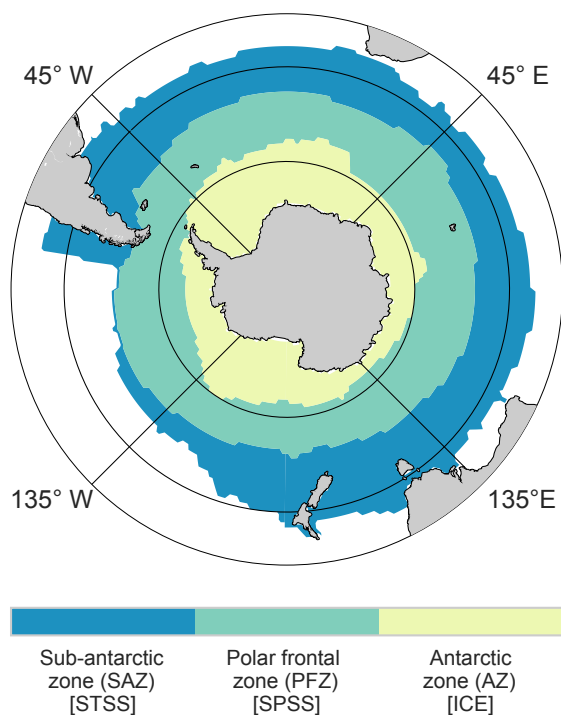


**Figure 1.** The three Southern Ocean biomes as defined by Fay and McKinley (2014). The common names for the biomes are shown in the key, with the abbreviations shown in the round brackets. The abbreviation in the square brackets show the abbreviations as given by Fay and McKinley (2014).

Sub-Antarctic Zone (SAZ); the sub-polar seasonally stratified biome (SPSS) becomes the Polar Frontal Zone (PFZ) and the ice biome (ICE) is the Antarctic Zone (AZ) (Mongwe et al., 2016).

The second part aims to better understand the limitations of these methods with the given dataset by implementing the methods with ocean biogeochemical model output. The domain of this synthetic data experiment is defined by the three southern biomes of Fay and McKinley (2014). These are defined by observed oceanographic and biological parameters, but are used for the sake of consistency despite potential differences between observations and the model.

## 2.1 Gridded data

The data sources are shown in Table 1. These gridded data refer primarily to remotely sensed data, with the exception of MLD and SSS. The latter variables are output from ECCO<sub>2</sub>, an assimilative model. The temporal range of the data (1998 through 2014) is limited by the availability of GlobColour (Chl *a* starting in 1998) and SOCAT v3 (*f*CO<sub>2</sub> ending in 2014).

All data are gridded to 1 month × 1° using *iris* and *xarray* packages in Python (Hoyer and Hamman, 2017; Met Office, 2017). Gridded *p*CO<sub>2</sub> (SOCAT v3) is used to train the algo-

rithms (Bakker et al., 2016). Surface station measurements (flask and tower) of atmospheric *x*CO<sub>2</sub> are interpolated to a regular grid using support vector regression (Masarie et al., 2014). Mean sea level pressure (NCEP2) is used in the conversion from *x*CO<sub>2</sub> to *p*CO<sub>2</sub> (Kanamitsu et al., 2002).

Cloud coverage and low light at high latitudes during winter result in missing Chl *a* data. Cloud gaps are filled with the climatology of Chl *a* (from 1998 to 2014) and missing low-light data are filled with a value of  $0.1 \pm 0.03 \text{ mg m}^{-3}$  (uniformly distributed random noise).

## 2.2 Model data

The output from a regional NEMO–PISCES configuration (BIOPERIANT05-GAA95b) is used as the synthetic dataset. The configuration is an updated version of PERIANT05 used by Dufour et al. (2012), where BIOPERIANT05-GAA95b includes biogeochemistry with PISCES-v2. The model has a peri-Antarctic domain with an open northern boundary at 30° S. The horizontal resolution of the configuration is  $0.5^\circ \cos(\text{latitude})$  with 46 vertical levels. The northern boundary is forced by a global  $0.5^\circ$  model, ORCA05 as presented in Biastoch et al. (2008). Output is saved as 5-day averages. The simulation was run from 1998 to 2009. The synthetic observations are sampled at the model resolution ( $5 \text{ days} \times 0.5^\circ$ ) to resemble the SOCAT dataset. Hereafter all data are resampled to  $1.0^\circ$  spatial resolution and monthly temporal resolution data to match observations. Finally, for the simulation experiment we define the Southern Ocean using the three southernmost biomes defined in Fay and McKinley (2014), as was done for the observational estimates.

## 2.3 Data transformation and derived variables

Both gridded data and synthetic input data are transformed in preparation for the empirical algorithms. The  $\log_{10}$  transformations of MLD and filled chlorophyll (Chl *a*<sub>clim</sub>) are taken to return a distribution that closer represents a normal distribution.

Several of the studies in Rödenbeck et al. (2015) included latitude, longitude and/or time as proxies of  $\Delta p\text{CO}_2$ . It is important to note that coordinates do not drive mechanistic changes in  $\Delta p\text{CO}_2$ . Rather, the inclusion of coordinates in the empirical methods account for unknown or regionally varying proxies that cannot be measured remotely. Many methods in the intercomparison by Rödenbeck et al. (2015) did not include coordinates, but account for unaccountable spatial variability by clustering or subsetting data regionally. In this study, we use a single large domain with no clustering or regional subsets. Two scenarios for each method in the simulation experiment are run: no coordinate variables, and including coordinate variables (time, latitude and longitude).

The coordinates are transformed to preserve the continuity of the data, as is shown below. Seasonality of the data is preserved by transforming the day of the year (*j*) and is included

**Table 1.** Information on data products used in this study. The temporal and spatial resolutions are for the raw data (before gridding). Dashes show that times are either not applicable or that the dataset is continually updated. Note that the start and end year show full years only. Links to download the data are given in the additional materials. The asterisk (\*) indicates that variables are the output of a data assimilative model.

| Group or product | Variables                       | Date range |      | Resolution |       | Reference                    |
|------------------|---------------------------------|------------|------|------------|-------|------------------------------|
|                  |                                 | Start      | End  | Time       | Space |                              |
| SOCAT v3         | $f\text{CO}_2^{\text{sea}}$     | 1970       | 2014 | 1 month    | 1°    | Bakker et al. (2016)         |
| CDIAC            | $x\text{CO}_2^{\text{atm}}$     | 1970       | 2014 | –          | –     | Masarie et al. (2014)        |
| GlobColour       | Chlorophyll                     | 1998       | –    | 1 day      | 0.25° | Maritorena and Siegel (2005) |
| GHRSSST          | Sea surface temperature         | 1981       | –    | 1 day      | 0.25° | Reynolds et al. (2007)       |
| ECCO2 (cube92)   | Mixed layer depth*<br>Salinity* | 1992       | 2015 | 1 day      | 0.25° | Menemenlis et al. (2008)     |

in both SVR and RFR analyses:

$$t = \begin{pmatrix} \cos(j \cdot \frac{2\pi}{365}) \\ \sin(j \cdot \frac{2\pi}{365}) \end{pmatrix}. \quad (1)$$

Transformed coordinate vectors were passed to both SVR and RFR using  $n$ -vector transformations of latitude ( $\lambda$ ) and longitude ( $\mu$ ) (Gade, 2010; Sasse et al., 2013), with  $n$  containing the following:

$$A, B, C = \begin{pmatrix} \sin(\lambda) \\ \sin(\mu) \cdot \cos(\lambda) \\ -\cos(\mu) \cdot \cos(\lambda) \end{pmatrix}. \quad (2)$$

Co-located  $f\text{CO}_2$  ( $y$ ) and proxy data ( $X$ ) are used to create training arrays ( $x$ ). The final input for SVR and RFR are (with 12 columns)  $\log_{10}(\text{Chl } a_{\text{clim}})$ , SST,  $f\text{CO}_2(\text{atm})$ , ADT,  $\log_{10}(\text{MLD})$ , ICE, SSS,  $\cos(j)$ ,  $\sin(j)$  and  $n$  vectors  $[A, B, C]$ . SVR requires each column of the proxies to be  $z$ -scored, i.e. normalized to the mean ( $\mu$ ) and standard deviation ( $\sigma$ ) of each column ( $\frac{x-\mu}{\sigma}$ ).

## 2.4 Empirical methods and implementation

Data are split randomly into a training and independent test dataset with a ratio of 0.7 : 0.3. The independent dataset is used to give a test error of the trained algorithm. The statistical learning package, scikit-learn, in Python is used for all regression and cross-validation methods (Pedregosa et al., 2011). The details on each cross-validation method are outlined in the subsections below.

### 2.4.1 Support vector regression

The basic formulation of SVR is similar to that of linear regression as described by Smola et al. (2004):

$$f(x) = \langle w, x \rangle + b \quad \text{with } b \in \mathbb{R}, \quad (3)$$

where  $b$  is an intercept and  $\langle \cdot, \cdot \rangle$  denotes the dot product of the weights ( $w$ ) and  $x$ , the training data. The weights and

intercept are found by solving the cost function:

$$\text{minimize } \frac{1}{2} \|w\|^2 \quad \text{subject to } \begin{cases} y_i - \langle w, x_i \rangle - b \leq \epsilon \\ \langle w, x_i \rangle + b - y_i \leq \epsilon \end{cases}. \quad (4)$$

In this form,  $w$  is minimized according to the target values ( $y_i$ ) to a precision of  $\epsilon$  – i.e. there is no room for error greater than  $\epsilon$ . However, with the majority of problems, meeting these constraints is not possible if data are noisy or  $\epsilon$  is set to be small. The inclusion of *slack variables* ( $\xi_i, \xi_i^*$ ) relaxes the constraints and the problem is now formulated as follows:

$$\text{minimize } \frac{1}{2} \|w\|^2 + C \sum_{i=1}^n (\xi_i + \xi_i^*)$$

$$\text{subject to } \begin{cases} y_i - \langle w, x_i \rangle - b \leq \epsilon + \xi_i \\ \langle w, x_i \rangle + b - y_i \leq \epsilon + \xi_i^* \\ \xi_i, \xi_i^* \geq 0 \end{cases}. \quad (5)$$

Here  $C$  is a parameter that adjusts for the amount of error that the minimization allows. The slack variable  $|\xi|$  is only counted towards the cost if the point lies outside the margin ( $|\xi| \geq \epsilon$ ). The points on or outside the margins are called support vectors and are used to construct the hypothesis function,  $h(x)$ . This is shown in Fig. 2a where a linear SVR is fitted to noisy data produced from a cubic spline. The optimization problem shown in Eq. (5) is solved in its dual formulation (see Hastie et al., 2009, for the full description). Importantly, solving the dual formulation allows for efficient kernelization of SVR.

Kernelization describes the process that maps the proxy variables ( $x$ ) onto a higher dimensional feature space. In this study we used a Gaussian kernel (or radial basis function – RBF), which allows for potentially infinite complexity determined by the number of support vectors (Vapnik, 1999). The RBF kernel introduces an additional hyper-parameter ( $\gamma$ ) that defines the width of the Gaussian. Selection of the SVR hyper-parameters ( $\epsilon$ ,  $C$ ,  $\gamma$ ) is done using a two-stage exhaustive grid search approach with cross-validation. We

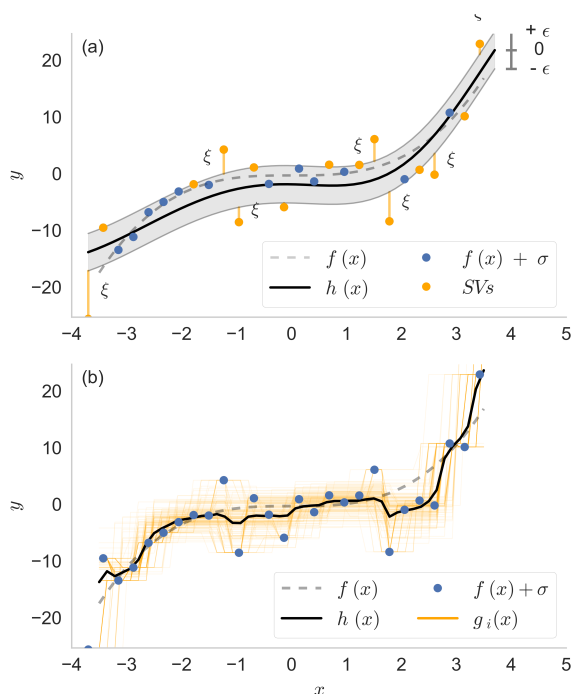


**Figure 2.** A simple example demonstrating the principle of (a) support vector regression and (b) random forest regression. The dashed grey line is the true function  $f(x) = 0.4x^3$  with the blue dots representing a random sample taken from this function  $f(x) + \sigma$ , where  $\sigma$  is normally distributed noise. The black line in each panel,  $h(x)$ , shows the estimate of the true function. The orange dots in (a) show the samples from the random subset chosen as support vectors from which  $h(x)$  is estimated. The orange lines in (b) show 200 decision tree estimates,  $g_i(x)$ , which are averaged to create the ensemble,  $h(x)$ .

use K-fold cross-validation, where the data are divided into eight equal “folds” ( $k = 8$ ). Seven of the folds are used to train the model, while the remaining fold is used for validation. This is done iteratively until each excluded fold has been used to test the results.

#### 2.4.2 Random forest regression

Decision trees form the basic building block of a random forest (RF), with the average of  $n$  decision trees taken as the ensemble estimate (Breiman, 2001) (Fig. 2b). The basic idea of a decision tree is to iteratively partition data into boxes using simple rules that minimize the error at each split (referred to as a node) – these boxes would become hypercubes in higher dimensional problems. This is described by the basic formulation as described in Loh (2011):

1. Start at the root node.
2. For each  $X$ , find the set  $S$  that minimizes the sum of the node impurities in the two child nodes and choose the split  $X \in S$  that gives the minimum overall  $X$  and  $S$ .

3. If a stopping criterion is reached, exit. Otherwise, apply step 2 to each child node in turn.

Decision trees have high variance due to their discrete nature. Random forests reduce this high variance by bootstrapping with aggregation (called *bagging*): a subset of the available training dataset is sampled with a replacement for each decision tree in the RF. The sampling with replacement means that each training observation has a  $\sim 63\%$  chance of being chosen at least once for a particular tree (Louppe, 2014). This subsampling provides estimates that are robust to outliers as these have a chance of being omitted in training. This means that a random forest typically performs better when number of decision trees ( $t$ ) is large, but increasing the number of trees has diminishing returns in terms of performance vs. computation. Additional robustness is given to RFs by randomizing and/or limiting the number of proxy variables ( $m$ ) given to the nodes in each tree when splitting the data (hence random) (Louppe, 2014). In this study, the maximum number of proxy variables ( $m = 11$ ) was given to the RFR. The complexity of a RF can be adjusted by limiting the minimum number of leaves at a terminal branch ( $l$ ), where a fully grown tree would allow  $l$  to be one.

A useful feature of bagging is that it intrinsically provides a cross-validation dataset (a.k.a. out-of-bag samples) that is not part of the training procedure (for a specific set of trees). The out-of-bag samples are those that are not selected during bagging. The advantage of this approach over K-fold cross-validation is that the full dataset can be used in the training procedure, as opposed to splitting the dataset for cross-validation. The out-of-bag error is used to cross-validate the model and select the hyper-parameters ( $t$ ,  $m$ ,  $l$ ) for the RF.

#### 2.5 CO<sub>2</sub> fluxes

Air–sea CO<sub>2</sub> fluxes are quantified with the following:

$$FCO_2 = K_0 \cdot k_w \cdot \Delta pCO_2 \cdot (1 - [\text{ice}]). \quad (6)$$

The gas transfer velocity ( $k_w$ ) is calculated using a quadratic dependency of wind speed with the coefficients of Wanninkhof (2014). The  $u$  and  $v$  vectors of CCMP v2 are used to compute the wind speed (Atlas et al., 2011). Coefficients from Weiss (1974) are used for  $K_0$  and  $\Delta pCO_2$  is estimated by the empirical models. The effect of sea-ice cover on CO<sub>2</sub> fluxes is treated linearly; the fraction of sea ice cover ([ice]) is converted to fraction of open water by subtracting 1 as shown in Eq. (6).

These results are analysed regionally with the three Southern Ocean biomes defined by Fay and McKinley (2014) (Fig. 1). We compare our estimates of CO<sub>2</sub> fluxes with those of Landschützer et al. (2014), who used a two-step neural network method abbreviated to SOM-FFN. Note that the SOM-FFN method was trained using SOCAT v2 compared to the methods in this study that used SOCAT v3.

## 2.6 Synthetic data experiments

Two experiments are run with the synthetic data. The first experiment aims to identify the efficacy of including or omitting coordinates as proxy variables on each method's ability to estimate  $\Delta p\text{CO}_2$  using SOCAT v3 locations. This is achieved by implementing the model with the transformed coordinate variables as proxies and then without. Note that the training procedure for the models remains the same as for the observational estimates of  $\Delta p\text{CO}_2$ .

The second experiment assesses the impact that the seasonally sparse SOCAT v3 has on the ability of the methods to estimate  $\Delta p\text{CO}_2$ . This is done by comparing the results of  $\Delta p\text{CO}_2$  estimates when trained according to (1) SOCAT v3 locations trained with synthetic data (Fig. 3a) and (2) uniformly random sampling locations (random in space and time) with a sample size the same as SOCAT v3 (Fig. 3b). Once again this the training procedure remains the same (as stated above).

## 3 Results

### 3.1 Observational CO<sub>2</sub> data results

We use the RMSE as the primary metric of the methods' performance as shown in Fig. 4a–c. Note that the RFR RMSE is calculated from the out-of-bag error (effectively an independent error). SOM-FFN has the best RMSE score of 14.84  $\mu\text{atm}$  (using SOCAT v2), which is better than the RMSE of RFR (16.45  $\mu\text{atm}$ ) and SVR (24.404  $\mu\text{atm}$ ), which are trained with SOCAT v3. The biases of the different methods are similar in magnitude for each of the biomes (−0.40, −0.03 and −0.75  $\mu\text{atm}$  for the SOM-FFN, RFR and SVR, respectively). The mean absolute errors (MAEs) for the respective methods are 9.78, 9.85 and 15.27  $\mu\text{atm}$ .

The difference between the MAE and the RMSE highlights the ability of methods to fit outliers or extreme points, as the RMSE metric penalizes outliers more severely than the MAE. The SOM-FFN approach has the smallest difference between these two metrics (5.06, 6.60 and 9.13  $\mu\text{atm}$  for the SOM-FFN, RFR and SVR, respectively). This superior performance may be due to two factors. Firstly, the SOM-FFN method may be better at fitting the extreme points (those that are in the outer percentiles of the distribution). Second, it may allude to the fact that the SOCAT v2 dataset is less variable. Testing the SVR and RFR implementations against SOCAT v2 yields similar results, with the exception of in the SAZ, where both RMSE and MAE improve (results shown in Table 2).

The RMSEs and biases in the PFZ are least variable between methods. While there is a substantial increase in the number of observations from 2004 there is no appreciable change in the RMSE. The Antarctic Zone (AZ) is the primary contributor to these errors with much larger average

**Table 2.** Various performance metrics for empirical estimates of  $\Delta p\text{CO}_2$  in the Sub-Antarctic Zone (SAZ), Polar Frontal Zone (PFZ) and Antarctic Zone (AZ) (as defined by Fay and McKinley, 2014). Results tested according to SOCAT v2 and SOCAT v3 are shown for the SVR and RFR methods.

|     | Method   | RMSE  | MAE   | $r^2$ | Bias  |
|-----|----------|-------|-------|-------|-------|
| SAZ | SVR (v3) | 18.14 | 11.28 | 0.48  | 0.61  |
|     | SVR (v2) | 15.99 | 10.36 | 0.49  | 0.20  |
|     | RFR (v3) | 13.67 | 8.16  | 0.70  | −0.14 |
|     | RFR (v2) | 12.66 | 7.65  | 0.68  | −0.29 |
|     | SOM-FFN  | 10.07 | 7.04  | 0.76  | −1.15 |
| PFZ | SVR (v3) | 14.45 | 10.06 | 0.48  | 0.31  |
|     | SVR (v2) | 14.29 | 10.01 | 0.44  | −0.01 |
|     | RFR (v3) | 10.71 | 6.7   | 0.71  | 0.21  |
|     | RFR (v2) | 10.56 | 6.77  | 0.69  | −0.34 |
|     | SOM-FFN  | 11.01 | 7.68  | 0.6   | 0.26  |
| AZ  | SVR (v3) | 36.14 | 25.19 | 0.56  | −3.22 |
|     | SVR (v2) | 35.69 | 25.01 | 0.59  | −2.88 |
|     | RFR (v3) | 23.8  | 15.81 | 0.8   | −0.27 |
|     | RFR (v2) | 23.49 | 15.63 | 0.81  | −0.62 |
|     | SOM-FFN  | 21.32 | 14.91 | 0.82  | −0.77 |

RMSE values than for the SAZ and PFZ (36.14, 23.80 and 21.32  $\mu\text{atm}$  for SVR, RFR and SOM-FFN, respectively). This increase in the RMSE is likely driven by the larger variability of  $\Delta p\text{CO}_2$  observations in the AZ, where standard deviations of observations are 25.05, 20.01 and 54.65  $\mu\text{atm}$  for the SAZ, PFZ and AZ, respectively. This is reflected in the highest  $r^2$  scores in the AZ for the respective methods (Table 2).

The annual and seasonal averages (winter = JJA, summer = DJF) for  $\Delta p\text{CO}_2$  estimated by RFR, SVR and SOM-FFN for the Southern Ocean are shown in Fig. 5. Note that the estimates have been scaled to sea ice concentration ( $\Delta p\text{CO}_2 \times (1 - [\text{ice}])$ ) as done for fluxes in Eq. (6) – this mutes winter estimates in the AZ. There is, in general, good agreement in the spatial distribution between the methods, with the SAZ being a net sink of CO<sub>2</sub> and the region south of the polar front (PFZ and AZ) being a source of CO<sub>2</sub> to the atmosphere, as found by Metzl et al. (2006).

More specifically, there is stronger zonal asymmetry in summer compared to winter. This is driven, in part, by a strong reduction of  $p\text{CO}_2$  by biological production (Metzl et al., 2006; Lenton et al., 2012). There are three regions in the SAZ where  $\Delta p\text{CO}_2$  reduction is strongest and consistent between methods (Fig. 5): east of South America (Brazil–Malvinas Confluence), south-east of Africa (Agulhas retroflexion) and between Australia and New Zealand (Tasman Sea). The reduction of  $\Delta p\text{CO}_2$  in the PFZ is strongest in the Atlantic sector downstream of the South Georgia and South Sandwich Islands and in the Indian sector downstream of the Kerguelen Plateau (Fig. 5d–f). In both cases, SAZ and PFZ, these regions are consistent with re-

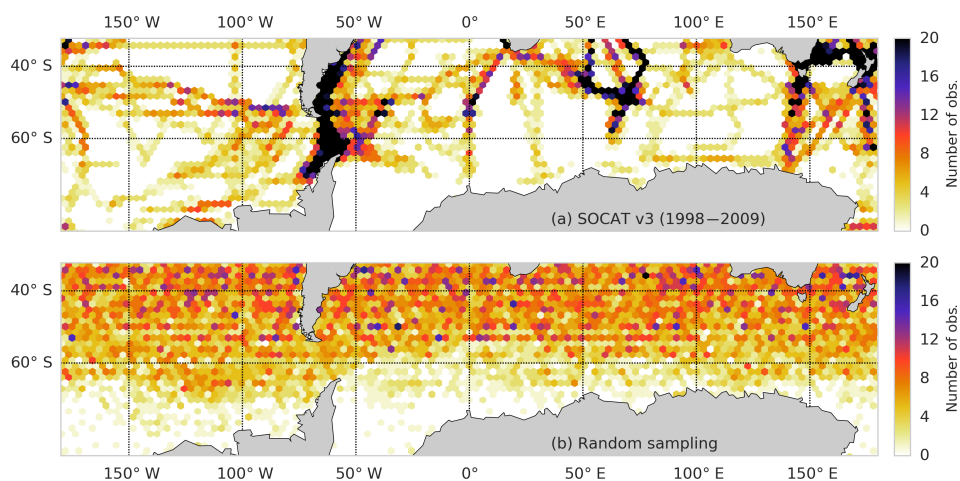


**Figure 3.** The spatial distribution of sampling locations in the synthetic dataset (BIOPERIANT05). The top panel (a) shows the sampling strategy using SOCAT v3 locations, and the bottom panel (b) shows the uniform random sampling distribution used in the second experiment.

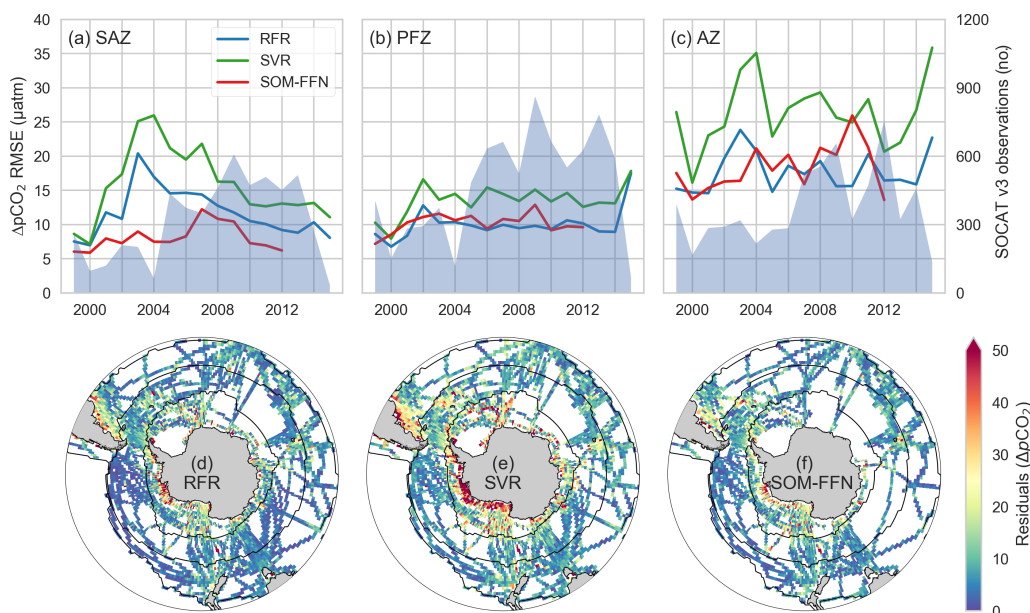


**Figure 4.** The RMSE (top row, a–c) for each of the three Southern Ocean biomes for RFR (blue), SVR (green) and SOM-FFN (red). The grey fill in the top row (a–c) shows the number of observations for each of the biomes for each year. The maps in the bottom row (d–f) show the spatial distribution of residuals in the Southern Ocean for SVR (d), SOM-FFN (e) and RFR (out-of-bag errors) (f). The thin black lines define the three Southern Ocean biomes as defined by Fay and McKinley (2014). Note that RFR and SVR are trained and tested with SOCAT v3 while SOM-FFN is trained and tested with SOCAT v2.

gions of high biomass (Thomalla et al., 2011; Carranza and Gille, 2015).

However, there are more subtle differences in the magnitudes and distributions of these patterns. The RFR underestimates winter outgassing south of the polar front (Fig. 5g) compared to the other methods, resulting in a weaker annual source. Conversely, the SVR has strong winter outgassing (Fig. 5h) in the PFZ compared to other methods. In summer, the largest difference occurs in the eastern Atlantic sector of the SAZ where the SOM-FFN  $\Delta p\text{CO}_2$  estimates (high-

lighted in Fig. 5f) are larger compared to SVR and RFR. Other differences in the spatial output are more subtle.

The agreements and differences between methods are also observed in the time series for each of the biomes (Fig. 6). Importantly, there is coherence in the strengthening sink (2002 to 2012) and timing of the seasonal cycle between the three methods (Landschützer et al., 2015). The differences in the magnitude of the winter outgassing in the PFZ and AZ (Fig. 6b, c) are also apparent, with the SVR overestimating

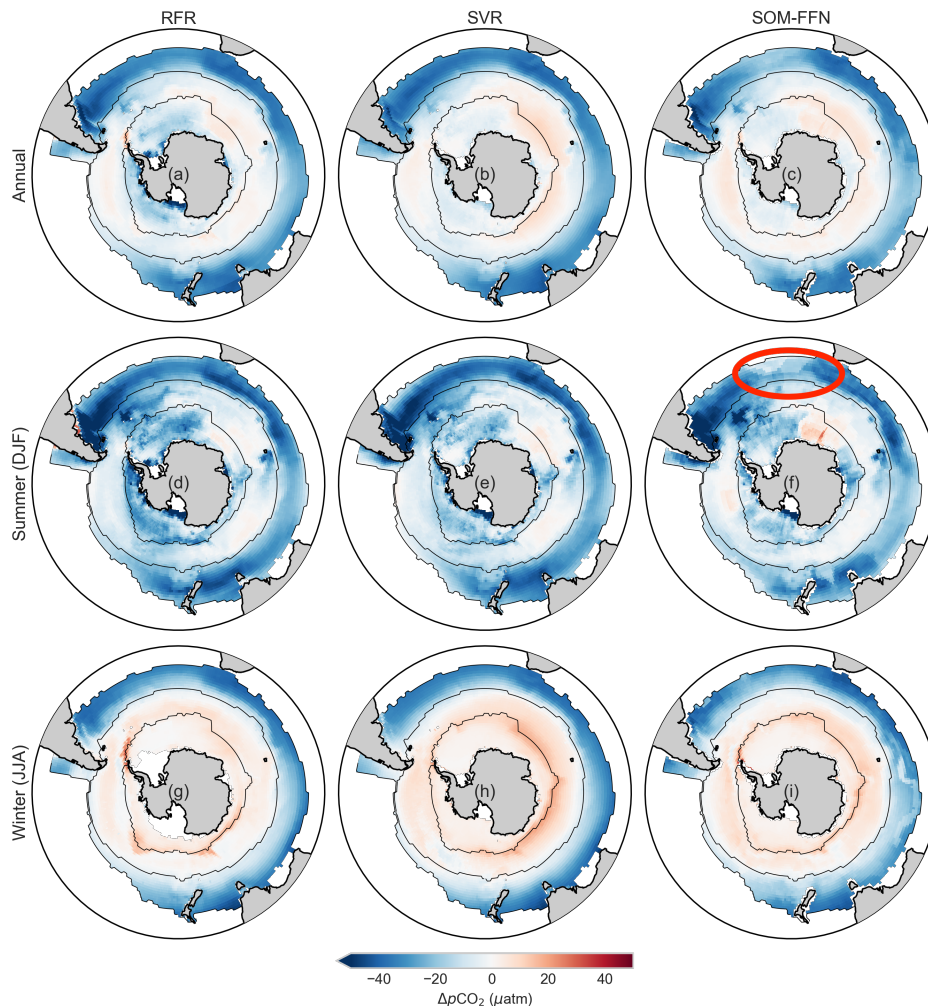


**Figure 5.** Seasonal averages for  $\Delta p\text{CO}_2$  from 1998 to 2014 for SVR, SOM-FFN and RFR. The annual mean is shown in the top row (a, b, c), the mean summer (DJF)  $\Delta p\text{CO}_2$  is shown in the middle row (d, e, f) and the mean winter (JJA)  $\Delta p\text{CO}_2$  is shown in the bottom row (g, h, i). The thin black lines denote the SAZ, PFZ and AZ from outside inward. Note that the  $\Delta p\text{CO}_2$  has been normalized to sea ice cover where  $\Delta p\text{CO}_2$  is multiplied by  $(1 - [\text{ice}])$ . The red oval in (f) highlights the difference in SOM-FFN estimates of  $\Delta p\text{CO}_2$  during summer in the Atlantic compared to SVR and RFR.

$\Delta p\text{CO}_2$  compared to other methods and the RFR with conservative outgassing estimates.

There is also a large difference between the SOM-FFN and the two other methods in summer, particularly from 1998 through 2006. Figure 5f shows that this could be driven by the difference in the eastern sector of the Atlantic (circled with red). Estimates of winter  $\Delta p\text{CO}_2$  are in agreement, with the exception of the last 4 years when SVR winter estimates increased relative to RFR. The SAZ and PFZ also show variability in the magnitude of a seasonal shoulder in late summer, where increasing  $\Delta p\text{CO}_2$  is briefly delayed by a short sharp decrease resulting in a saw-tooth pattern. This effect is the strongest for the SVR and weakest for the RFR.

The seasonal amplitude of  $\Delta p\text{CO}_2$  in the AZ is far larger than in the SAZ and PFZ (Fig. 6c) resulting in large method-

ological differences. However, this large differential is not realized in calculated air–sea CO<sub>2</sub> fluxes due to ice cover, as shown by the dashed lines (Fig. 6c). Summer estimates are also influenced by sea ice cover, but not to the extent that winter fluxes would be reduced.

### 3.2 Simulation experiment results

The advantage of using synthetic data is that both in- and out-of-sample errors can be estimated, where the in-sample error is calculated from the training points and the out-of-sample error is from the entire predicted domain. The latter gives a representation of the *true* error of the method. The results from these experiments are shown in Table 3. The detailed out-of-sample histograms are shown in Fig. B1.



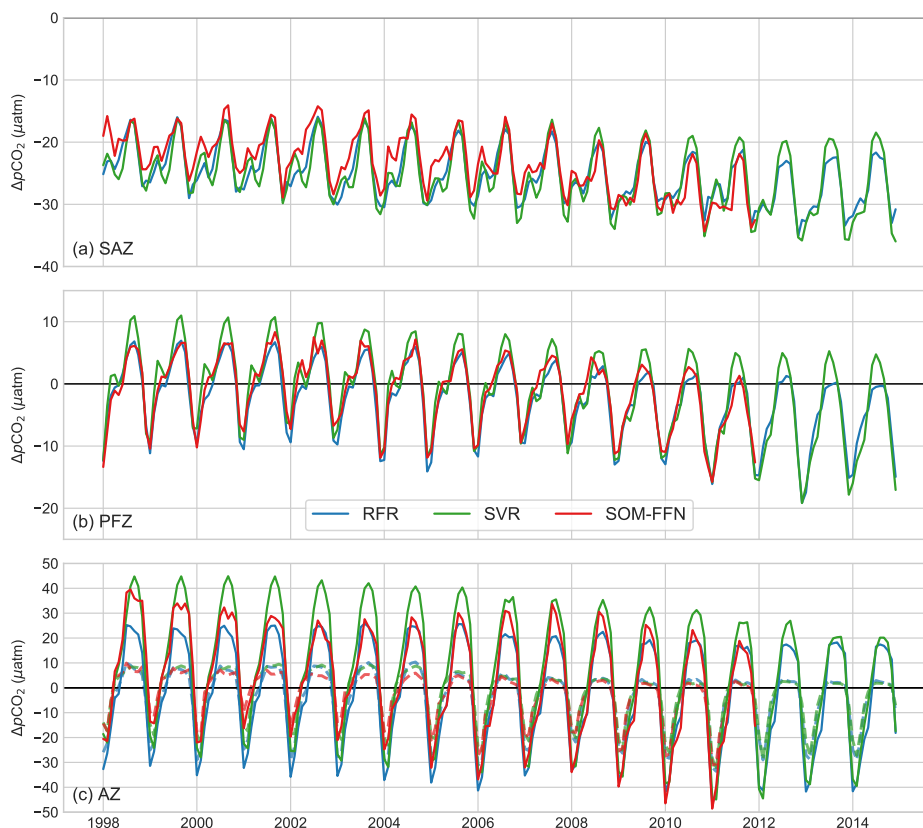


**Figure 6.** Time series of  $\Delta p\text{CO}_2$  estimates for the three Southern Ocean biomes as defined by Fay and McKinley (2014): SAZ, PFZ and MIZ. The y-axis grid lines represent the same scale for figures (a) through (c). The SOM-FFN estimates are only available until 2011 as it is trained with SOCAT v2, while the SVR and RFR are trained with SOCAT v3. The  $\Delta p\text{CO}_2$  normalized to sea ice cover is shown by dashed lines in the AZ.

**Table 3.** Root mean squared error (RMSE,  $\mu\text{atm}$ ) for the three synthetic data experiments for RFR (left), SVR (middle) and the ensemble mean (ENS) of the two methods. Both in- and out-of-sample errors are reported ( $E[\text{in}]$  and  $E[\text{out}]$ , respectively). SOCAT experiments are those where the location of synthetic training data is the same as SOCAT v3. This was run with (with coordinates) and without coordinates (without coordinates), namely time, latitude and longitude. A third experiment was run with random samples – coordinate variables are included as proxies.

| Experiment      |                             | RFR  | SVR  | ENS  |
|-----------------|-----------------------------|------|------|------|
| $E[\text{in}]$  | SOCAT (without coordinates) | 6.65 | 7.47 | –    |
|                 | SOCAT (with coordinates)    | 5.12 | 5.10 | –    |
|                 | Random Sampling             | 7.23 | 7.83 | –    |
| $E[\text{out}]$ | SOCAT (without coordinates) | 7.46 | 7.46 | 7.08 |
|                 | SOCAT (with coordinates)    | 5.76 | 6.19 | 5.36 |
|                 | Random sampling             | 4.88 | 4.94 | –    |

### 3.2.1 Coordinates as proxy variables

This experiment used the synthetic dataset to test the influence of including or excluding transformed coordinates (time, latitude and longitude) as proxies of  $\Delta p\text{CO}_2$ . There are four major results from the experiment results. Firstly, the RMSE estimates are smaller when coordinates are included as proxies for both in- and out-of-sample subsets (Table 3). Secondly, RFR achieves marginally better out-of-sample RMSE than SVR (5.76 and 6.19  $\mu\text{atm}$ , respectively) when trained with coordinates. Third, both RFR and SVR have comparable out-of-sample RMSE estimates (7.46  $\mu\text{atm}$ ) for  $\Delta p\text{CO}_2$  estimates trained with and without coordinate proxies. Lastly, the ensemble mean of SVR and RFR has lower out-of-sample RMSE estimates than the individual estimates for implementations with and without coordinate proxies, though these gains are marginal (Table 3).

These points can also be gleaned from RMSE maps (Fig. 7). Both RFR and SVR errors are low; however, the RFR outperforms the SVR marginally for the open-ocean regions. Errors in coastal regions remain high for each of the experiments and methods (Fig. 7a, b, d, e), such as in the

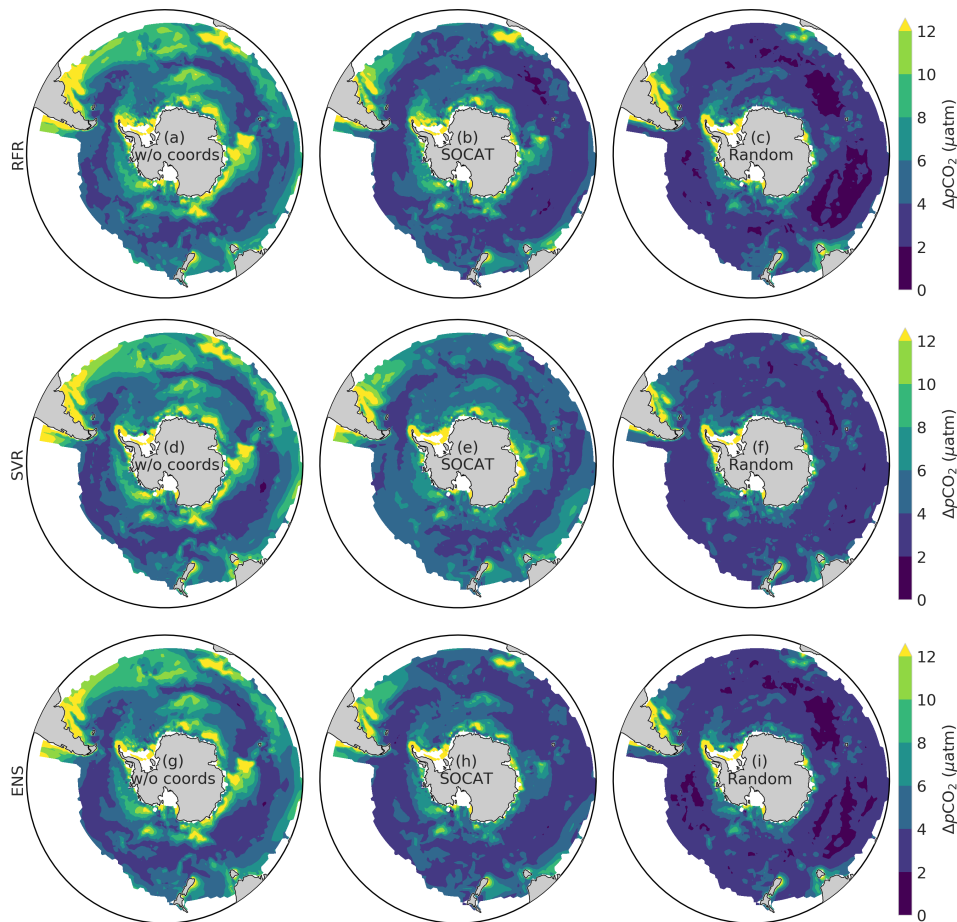


**Figure 7.** Distributions of root mean squared error (RMSE) for the three synthetic data experiments for RFR in the top row (a–c), SVR in the middle row (d–f) and the ensemble mean for RFR and SVR in the bottom row (g–i). The first column (a, d, g) shows the RMSE for synthetic SOCAT training locations without coordinates (w/o coords) as proxies, while the second column (b, e, h) includes coordinates as proxies. The last column (c, f, i) shows the RMSE of randomly sampled training locations where coordinates are included as proxies.

Argentine Sea, the Agulhas retroflection, and the marginal ice zone. The ensemble mean of the estimates achieves a balance between the two methods with low and moderate RMSE scores in the open-ocean and coastal regions. Lastly, the distributions of the errors for RFR and SVR without coordinate proxies (and thus the ensemble mean) are similar.

The time series (Fig. 8) show that including coordinate variables plays an important role in achieving accurate phasing of the seasonal cycle. When coordinates are not included as proxies, the phasing shifts earlier for both methods. There is also an improvement of estimates over time, where the first 2 years (1998 and 1999) have worse estimates for both SVR and RFR (Fig. 8). This does not seem to be linked to the number of observations, but could be due to the distribution. The ensemble  $\Delta p\text{CO}_2$  in the 1998 to 1999 period is closer to BIOPERANT05 output as the over- and underestimates of RFR and SVR, respectively, compensate for each other.

### 3.2.2 Random sampling regime

A second experiment is performed to assess the inaccuracies that arise due to the spatial and temporal sampling biases in the SOCAT v3 dataset. Training locations are chosen at random and uniformly in time and space. This eliminates any summer–winter biases as well as clustering of cruise tracks in certain regions (such as the Argentine sea). Note that coordinates are included as proxies of  $\Delta p\text{CO}_2$  with the random sampling regime.

Firstly, the results show that the biases in SOCAT v3 do contribute to out-of-sample errors, as the random sampling regime achieved lower RMSE scores than any of the other experiments (4.88 and 4.94  $\mu\text{atm}$  for RFR and SVR, respectively, as in Table 3). However, RFR is marginally less susceptible to sampling biases than SVR, as the relative improvement for the latter is larger (with differences of 0.88 and 1.70  $\mu\text{atm}$ , respectively). The spatial distributions of RMSE for the random sampling implementations (Fig. 7c, f) show

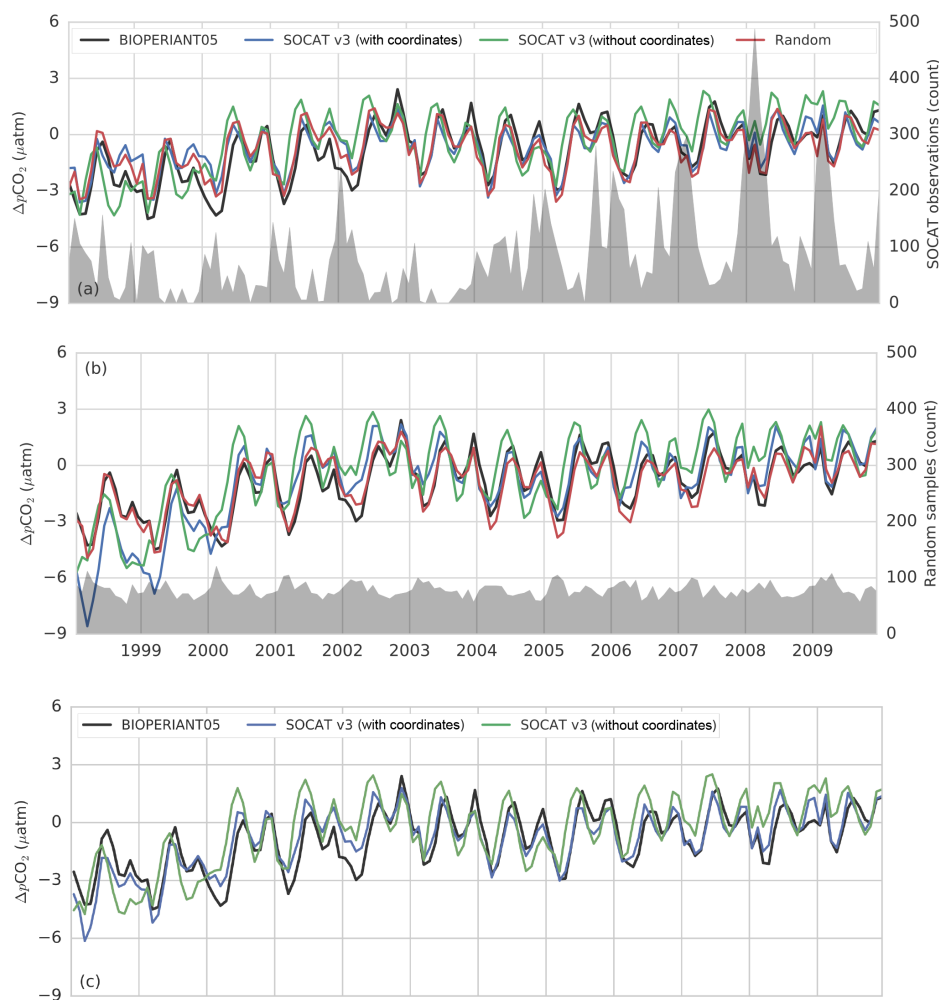


**Figure 8.** Time series of BIOPERIANT05  $\Delta p\text{CO}_2$  (target) and empirical estimates of  $\Delta p\text{CO}_2$  for each of the experiments for RFR (a), SVR (b) and the ensemble mean estimates (c). The SOCAT v3 estimates are trained using the locations of SOCAT v3 data. The variant *with coordinates* includes coordinates as proxies of  $\Delta p\text{CO}_2$  while these are not included for the variant labelled as *without coordinates*. The *Random* estimates are trained with uniformly distributed random sample locations. The number of samples per time step for SOCAT (a) and random sampling locations (b) are shown by the grey fill.

that errors in coastal regions remain high ( $> 12 \mu\text{atm}$ ) with uniform sampling. Lastly, there is an improvement in the estimates from 1998 to 2000, particularly with the random sampling for the SVR (Fig. 8), suggesting that the method is more susceptible to the temporal bias than RFR (if coordinates are included as proxies).

## 4 Discussion

### 4.1 Observational estimates

In this section we address the methods' ability to fit the training data, in other words an assessment of in-sample errors (Fig. 4 and Table 2). Thereafter we investigate the differences in the estimates of  $\Delta p\text{CO}_2$  (Figs. 5 and 6).

#### 4.1.1 Assessment of in-sample errors

Based on the results, the SOM-FFN method (by Landschützer et al., 2014) proves to be an elegant implementation of neural network methods that is able to estimate SOCAT  $\Delta p\text{CO}_2$  (in-sample estimate) better than the RFR and SVR methods (with respective RMSE estimates of 14.84, 16.45 and  $24.40 \mu\text{atm}$ ). Here we assess these differences and try to identify the possible reasons for the differences.

One of the largest differences in the methods' ability to fit the training data is in the SAZ where the RFR and SVR score poorly in comparison to SOM-FFN, particularly from 2000 to 2006 (Fig. 4a). This is during a period where the number of observations are still relatively low in the SOCAT v3 database (Fig. 4a). This may then be due to an increase in the complexity of  $\Delta p\text{CO}_2$  measurements in the SAZ from SO-

CAT v2 to v3 from 1998 through 2006, which makes the data more challenging to fit accurately. This is exemplified in the maps of RMSE (Fig. 4g–i), where coastal regions typically have larger error estimates. A comparison of SOCAT v2 and v3 for this period shows that the increase in the number of observations occurs primarily in the Argentine Sea, thus confirming this hypothesis (Fig. A1a). The comparison of SOCAT v2 and v3 RMSE results for RFR and SVR confirm this (Table 2), where there is a marked improvement when using the older dataset. Importantly, this shows that increasing the number of measurements does not necessarily improve the in-sample error estimates, but may yield a more accurate out-of-sample estimate; however, this is difficult to test with limited data.

Despite the improvement in performance when testing against SOCAT v2, SVR and RFR still have poorer performance than the SOM-FFN approach. We attribute this in part to the SOM-FFN's ability to reduce the large RMSE contributions observed in the other two methods. This notion is supported by the smaller difference between RMSE and MAE, especially in the SAZ (Table 2). The SOM-FFN achieves this by increasing the flexibility of the algorithm by having multiple regression models that can each be optimized for data with a particular length scale of variability. This allows the SOM-FFN approach to adapt to short scales of variability in dynamic regions such as the Argentine Sea and the coastal Antarctic (Fig. 4i).

In comparison, this implementation of SVR, which is theoretically similar to an artificial neural network, only has one length scale for the entire domain (Vapnik, 1999; Smola et al., 2004). This becomes apparent in the AZ, where many of the observations are in the more biogeochemically dynamic coastal Antarctic, where melting sea ice results in short decorrelation length scales (Bakker et al., 2008; Chierici et al., 2012; Jones et al., 2012). The SVR has much larger RMSE scores in the AZ than the RFR or SOM-FFN (35.69, 23.49 and 21.32  $\mu\text{atm}$ , respectively). This suggests that implementing the SVR approach without an initial clustering or regionalization step will not yield good results.

By comparison, the RFR approach is more adept at fitting various length scales of variability, accounting for both the higher and lower variability in the AZ and PFZ, respectively (with SOCAT v3 standard deviations of 54.65 and 20.01, respectively). The high  $r^2$  scores achieved by RFR in the AZ and PFZ (0.81 and 0.71, respectively) highlight the flexibility in the method (Table 2). This is due to the differences in the underlying mathematics of the methods. Decision trees, which are the building blocks of RFR, separate data at each decision node with a discrete boundary (Breiman, 2001). Conversely, ANNs and SVRs often use Gaussian functions in the cost function, resulting in smoother approximations (Vapnik, 1999). This makes decision trees prone to overfitting, but the ensemble implementation of random forests eliminates this to a large extent.

#### 4.1.2 Differences in $\Delta p\text{CO}_2$ estimates

One of the largest differences in  $\Delta p\text{CO}_2$  is the weaker sink estimated by the SOM-FFN method in the SAZ (Fig. 6). This difference can be traced to the eastern Atlantic SAZ, where the SOM-FFN has higher estimates of  $\Delta p\text{CO}_2$  (Fig. 5e shown by the red oval and the differences between the methods in Fig. A3a, b). A comparison between the SVR and RFR trained with SOCAT v2 and v3 further eliminates the use of different training datasets as primary sources of difference, where methodology is a higher-order driver of difference (Fig. A2). The lack of this feature in the eastern Atlantic sector of the Southern Ocean in SVR and RFR estimates suggests that this is a function of the initial clustering step in the SOM-FFN. The clustering process separates  $p\text{CO}_2$  observations into clusters that are not restricted in time and space (Landschützer et al., 2014). This allows the SOM-FFN to “transfer knowledge” from a remote location (even outside the Southern Hemisphere) if proxies are similar to the Southern Ocean. This knowledge transfer assumes that the relationship between  $p\text{CO}_2$  and the measured proxies is globally consistent. Moreover, there is the assumption that all  $p\text{CO}_2$  variability (within a cluster) can be captured by the measured proxies. This assumption is not made when using coordinates or regional subsets as locations are isolated, but there is then the potential loss of knowledge from remote locations. This question will be addressed further in the discussion on the use of coordinate variables as proxies of  $\Delta p\text{CO}_2$ .

Another difference between  $\Delta p\text{CO}_2$  estimates is the tendency for SVR to overestimate  $\Delta p\text{CO}_2$  relative to the RFR and SOM-FFN approaches, particularly in the PFZ and AZ where winter data are sparse (Fig. 6b, c). We attribute this to the SVR's sensitivity to outliers, determined by the fact that the cost function penalizes outliers heavily (Eq. 5). In context of the SOCAT v3 dataset, the algorithm may treat the sparse winter data as outliers. This is due to the fact that sparse winter measurements of  $\Delta p\text{CO}_2$  are positive, while the abundant summer measurements are negative (Metzl et al., 2006; Lenton et al., 2013). This may then be a positive realization of a methodological attribute that is typically considered a weakness.

Conversely, RFR winter estimates of  $\Delta p\text{CO}_2$  are often lower than the SOM-FFN and SVR estimates, again in the AZ and PFZ (Figs. 5g–i and 6b, c). This may be due to the method's resilience against outliers, which could be due to two attributes (Louppe, 2014). Firstly, outliers are less likely to dominate the feature space with the use of bootstrap aggregation as these points will be sampled less frequently. Secondly, individual decision trees regress values by using the average of samples in a terminal node (or leaf), where the minimum number of samples per terminal node is set by the user. This second attribute means that estimates will never be outside the bounds of the minimum and maximum of the training dataset, thus leading to conservative estimates (as shown in Fig. 2b). The differences between the methods

shown in Fig. 6 could be a good case for an ensemble approach, where the strengths of one model compensate for the weakness of another. This is assessed in the synthetic data and will be discussed further.

These attributes may also be the reason for the differences in the magnitudes of the autumn peak in  $\Delta p\text{CO}_2$  in the SAZ and PFZ. Mechanistically this peak could be attributed to a sharp increase in cooling leading into winter, resulting in increased solubility of CO<sub>2</sub> and thus a sharp reduction of  $\Delta p\text{CO}_2$  (Metzl et al., 2006; Takahashi et al., 2002). Deeper mixing of the water column shortly thereafter would entrain CO<sub>2</sub>-rich waters, thus increasing  $\Delta p\text{CO}_2$  (Lenton et al., 2013). However, the trend for this peak to shrink in the SAZ and PFZ for all methods suggests that this may be an artefact that is specific to the SOCAT dataset.

## 4.2 Synthetic data experiments

In this section we discuss the outcomes of the two experiments performed on the synthetic dataset (BIOPERIANT05 model output). The first experiment addresses the efficacy of including coordinate variables as proxies of  $\Delta p\text{CO}_2$ . This is done by running two implementations of RFR and SVR: without coordinates as proxies, and with coordinates as proxies. The second experiment addresses the impact that the SOCAT dataset, biased in both space and time has on  $\Delta p\text{CO}_2$  estimates.

### 4.2.1 Coordinate variables improve estimates

This topic has to some extent already been mentioned in the discussion of the observational data, in which the cases for and against the inclusion of coordinate variables as proxies for  $\Delta p\text{CO}_2$  were put forward. If coordinates are not included there is the benefit of potential information transfer from remote parts of the domain, but this assumes that the satellite observable proxies (and assimilative model output) constrain  $\Delta p\text{CO}_2$  in a globally consistent way. If coordinates are included the information transfer is lost and the assumption is made that the proxy variables are not able to constrain  $\Delta p\text{CO}_2$  in a globally consistent manner.

The results of this experiment show that coordinates improve estimates of  $\Delta p\text{CO}_2$  with better RMSE scores for both SVR and RFR (Table 3). We are thus in favour of the second hypothesis that the available proxies cannot sufficiently constrain  $\Delta p\text{CO}_2$  without coordinates. A two-step clustering approach, such as SOM-FFN, may be able to achieve comparable results without coordinates, but this would have to be tested with that specific method. However, this may also lead to trends in the data that may be artefacts of remote knowledge transfer, as potentially seen in the observational data (Fig. 5f).

An important outcome of this experiment is that the inclusion of coordinates improves the seasonal phasing of the methods (Fig. 8a, b). It is critical for the empirical methods

to correctly estimate the phasing of  $\Delta p\text{CO}_2$  as the seasonal cycle phasing may be a useful indicator of anthropogenically driven changes to the marine carbonate system.

One of the assumptions in these synthetic data experiments is that the models are, to some extent, representative of the variability in the observed ocean. However, the BIOPERIANT05 output does not achieve this, with a standard deviation of 19.80  $\mu\text{atm}$  for synthetic SOCAT v3 data compared to 38.20  $\mu\text{atm}$  of the gridded SOCAT v3 observations (according to Southern Ocean as defined by Fay and McKinley, 2014). This could be a cause for concern. However, we believe that this creates an even a stronger case for the use of coordinates as proxy variables. The increased variability in the observations could be due to processes that deterministic models cannot yet constrain due to our lack of understanding of the marine carbonate system (Lenton et al., 2013; Mongwe et al., 2016).

### 4.2.2 SOCAT biases

The lack of winter  $p\text{CO}_2$  data is a problem throughout the mid-latitude and high latitude oceans, but is particularly severe in the Southern Ocean (Bakker et al., 2016), and the impact of the lack of data in the Southern Ocean is not known. Moreover, the efficacy of various methods to fill this large temporal gap is unknown (Rödenbeck et al., 2015). Here we show that there is a considerable impact in this synthetic data environment, but the effect of the sampling bias is perhaps smaller than we would have anticipated. Both methods are able to estimate the spatial distribution and the seasonal cycle of  $\Delta p\text{CO}_2$  with relative accuracy (Figs. 8 and 7 and Table 3). This could be due to two factors.

Firstly, winter data are less variable than summer data and require less sampling. Mechanistically, this is a likely scenario. In summer  $\Delta p\text{CO}_2$  is spatio-temporally heterogeneous in the Southern Ocean due to the uptake of CO<sub>2</sub> by phytoplankton (Metzl et al., 2006; Bakker et al., 2008; Thomalla et al., 2011; Chierici et al., 2012; Lenton et al., 2013). The drivers of phytoplankton are complex due to the co-limitation of light and iron (as a micronutrient) in the Southern Ocean (Boyd and Ellwood, 2010; Thomalla et al., 2011; Tagliabue et al., 2014). This complexity would require more sampling: perhaps additional proxies or increased spatial resolution to capture the variability of  $\Delta p\text{CO}_2$ . Conversely, processes driving winter  $\Delta p\text{CO}_2$ , namely the interaction of mixing and buoyancy, act on larger scales, potentially leading to less spatio-temporal heterogeneity. However, the lack of observations means that we simply cannot know with certainty. This makes a strong case for autonomous sampling platforms to the Southern Ocean's winter sampling gap. The SOCCOM float project may soon yield such measurements with pH-derived estimates of  $p\text{CO}_2$  (Russell et al., 2014; Johnson et al., 2017; Williams et al., 2017).

Secondly, the model used to generate the synthetic data may not be representative of the Southern Ocean. This has

been discussed in the previous section, but here, rather than increasing our confidence, it diminishes our confidence in the result. Studies have shown that process models are not able to accurately represent the seasonal cycle of CO<sub>2</sub> in the Southern Ocean (Lenton et al., 2013; Mongwe et al., 2016). Moreover,  $\Delta p\text{CO}_2$  is often driven by processes that are not representative of observations (Mongwe et al., 2016).

The most likely scenario is likely a combination of these two factors, where winter data are in fact less variable than summer data, but the error is larger than the experiment shows due to incomplete knowledge of the processes that describe  $p\text{CO}_2$  in the process models.

#### 4.2.3 The best method: the ensemble average

The synthetic data also allow us to compare the two methods relative to each other, in the context of the SOCAT v3 data. The data show that the RFR method performs better than the SVR (trained with coordinates as proxies) with respective out-of-sample RMSEs of 5.76 and 6.19  $\mu\text{atm}$  (Table 3). However, it is the average of these two methods (ensemble mean) that achieves the lowest RMSE (5.36  $\mu\text{atm}$ ), albeit marginal. The time series in Fig. 8c shows that the improvement may come from the period 1998 to 2000, when RFR is plagued by underestimation of the sink strength, while SVR overestimates the sink strength. This supports the notion that the strengths and weaknesses of these two methods compliment each other. Moreover, it supports the merit of multiple approaches and further development of empirical methods for the estimation of  $\Delta p\text{CO}_2$ .

## 5 Conclusions

In this study two empirical methods (SVR and RFR) are presented as alternative and complementary  $p\text{CO}_2$  gap-filling methods. These algorithms are established in other fields, but have not been applied for the estimation of surface ocean  $\Delta p\text{CO}_2$ . We apply the methods to the Southern Ocean where the paucity of ship-based measurements during winter is one of the major challenges. The SOCAT v3 dataset was co-located with assimilative model output and satellite measurable proxy variables to create a training dataset (Bakker et al., 2016). These estimates were compared with the SOM-FFN approach by Landschützer et al. (2014).

We found that the SOM-FFN and RFR methods had error estimates of similar magnitudes, while SVR had a larger error estimate. The RFR performed comparably to the SOM-FFN approach when compared with the SOCAT v2 dataset, with which SOM-FFN was trained. The increase in the num-

ber of measurements in the highly variable coastal ocean between SOCAT v2 and v3 leads to increased RMSE values, particularly in the Sub-Antarctic Zone (SAZ). Despite accounting for the increase in coastal data, the SOM-FFN had error estimates comparable to RFR and SVR the approach in the SAZ. We attribute this to the method's ability to cluster the training data into regions of different modes of variability to which individual regressions are then applied. The SVR method performed poorly due to its inability to adapt to various modes of variability, while the RFR is intrinsically much more flexible and thus performed well in fitting the training data.

There was good agreement amongst the three methods with respect to the overall trend of  $\Delta p\text{CO}_2$ , but there were also differences. The primary difference was in the Atlantic sector of the SAZ, where the SOM-FFN overestimated  $\Delta p\text{CO}_2$  relative to the other methods. This is likely due to remote knowledge transfer within a data-sparse cluster; however, we cannot identify this as right or wrong due to the lack of data in this region. Other differences were due to intrinsic attributes of the methods: SVR was sensitive to outliers, resulting in relatively large winter  $\Delta p\text{CO}_2$  estimates – potentially a desirable feature for sparse winter data; RFR underestimated  $\Delta p\text{CO}_2$  relative to the other methods due to its robustness to outliers.

To test the efficacy of these methods, they were applied to a synthetic dataset (process model output). Two major questions were asked: (1) what is the efficacy of including coordinate variables (time, latitude and longitude) as proxy variables? (2) What is the impact of sampling biases in the SOCAT v3 dataset? The results showed that including coordinate variables improved the estimates of  $\Delta p\text{CO}_2$  for SVR and RFR. Moreover, the phasing of the seasonal cycle was also improved with the inclusion of coordinates. The second experiment showed that there is only a small bias in the estimates of  $\Delta p\text{CO}_2$ ; however, the inability of process models to represent Southern Ocean  $\Delta p\text{CO}_2$  variability accurately places uncertainty on this result.

Lastly, we show that while the RFR approach outperforms the SVR approach, the ensemble mean of the two methods scores better than either individual methods. This provides a motivation for continued research on methods that complement each other in strengths and weaknesses.

*Data availability.* The data are available at <https://doi.org/10.6084/m9.figshare.5369038> (Gregor et al., 2017).

### Appendix A: Comparison of SOCAT v2 and v3

One of the shortcomings of this study is that the SOM-FFN method used SOCAT v2 as a training dataset, while the SVR and RFR methods were trained with SOCAT v3. Figure A3 shows that there is a marked difference between the two datasets. Importantly, the increase in the number of observations between 1998 and 2006 between SOCAT v2 and v3 are almost exclusively in the Argentine Sea.

These differences may have an impact on the estimates of  $\Delta p\text{CO}_2$ . To test this, the methods were implemented as explained in Sect. 2.4 with the exception that RFR and SVR methods were trained with both SOCAT v2 and v3. Figure A2 shows that, on average, there is a larger difference between the RFR and SVR methods than the different training datasets.

The differences between the different methods are shown in Fig. A3. Figures (a) and (b) show that the SVR and RFR methods estimate a stronger sink in the Atlantic sector of the SAZ. Here (Fig. A3b) the tendency of the SVR method to estimate strong outgassing south of the polar front relative to SOM-FFN and RFR is also seen. Conversely, the RFR, on average, underestimates  $\Delta p\text{CO}_2$  south of the polar front.

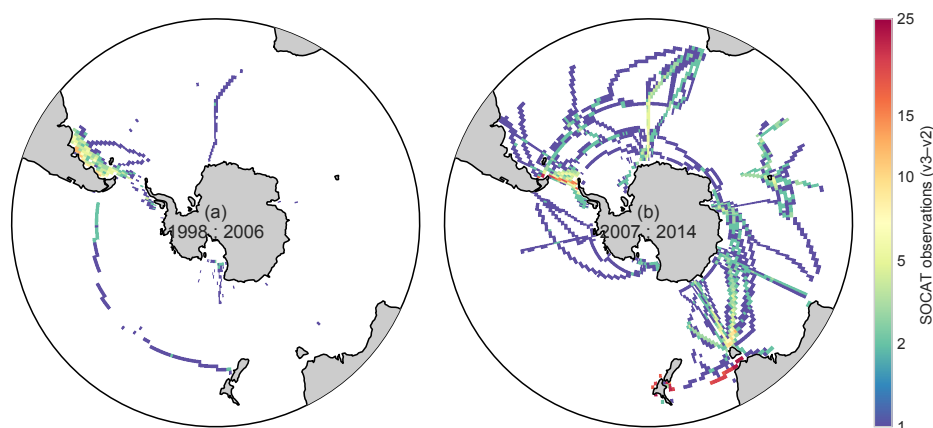


**Figure A1.** The increase in the number of observations between SOCAT v2 and SOCAT v3 for two periods: (a) 1998 through 2006, and 2007 through 2014.

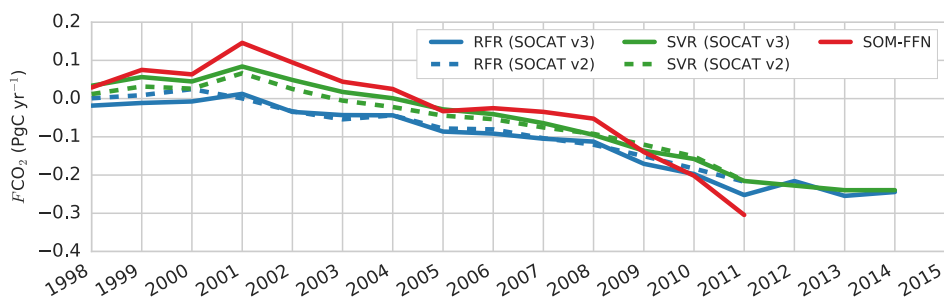


**Figure A2.** Comparison of air–sea CO<sub>2</sub> flux RFR and SVR when trained with SOCAT v2 and v3. The SOM-FFN method, trained with SOCAT v2, is also shown. The figure demonstrates that methodology plays a larger role in determining the outcome of the estimate than the availability of data (for these two methods).

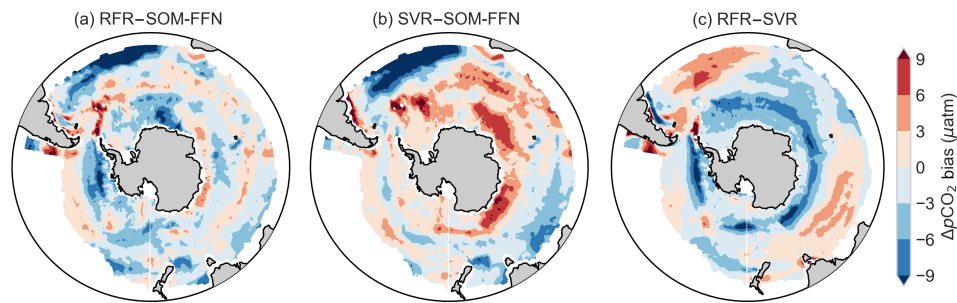


**Figure A3.** The differences between annual averages of each of the approaches for the period 1998 to 2006: (a) RFR–SOM-FFN; (b) SVR–SOM-FFN; (c) RFR–SVR.

## Appendix B: Synthetic data experiments

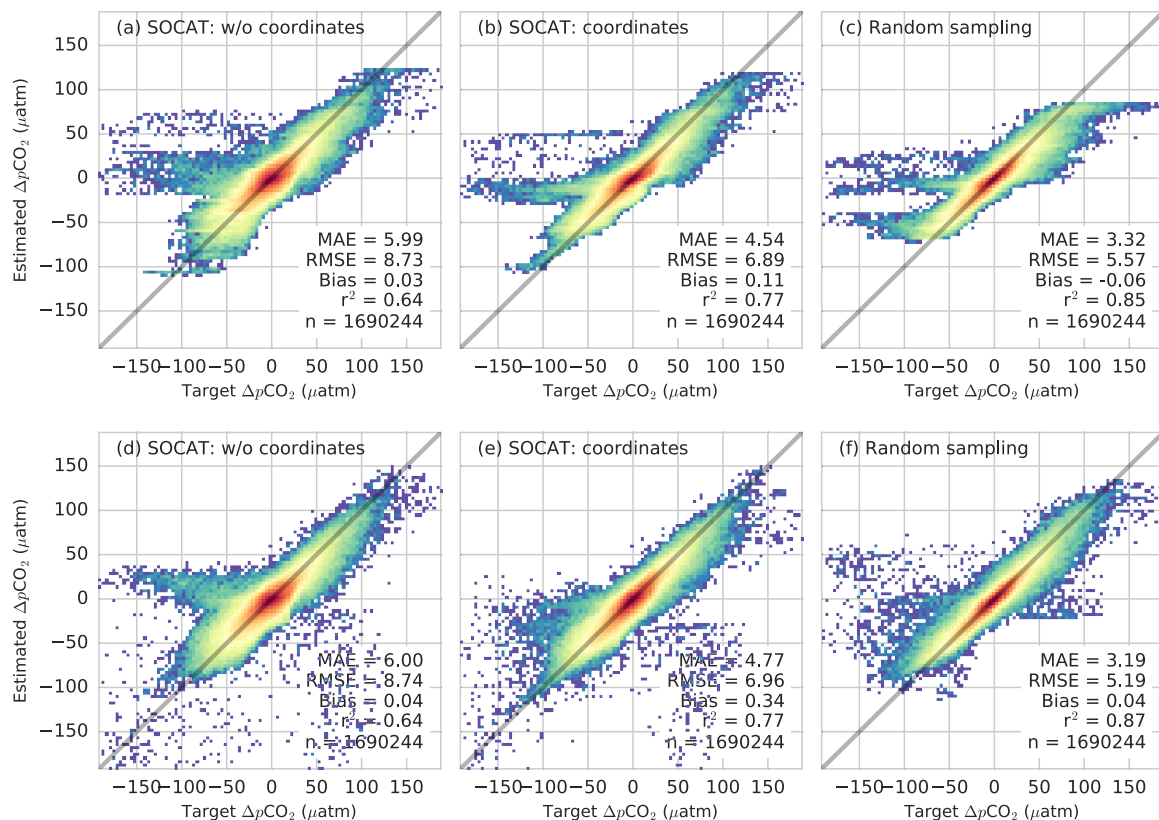


**Figure B1.** Two-dimensional histograms for the distributions of out-of-sample estimates of  $\Delta p\text{CO}_2$  relative to target  $\Delta p\text{CO}_2$  (BIOPERI-ANT05). The top row (a–c) shows estimates made by RFR and the bottom row (d–f) shows estimates of SVR. The first column (a, c) shows those estimates trained SOCAT v3 locations without coordinate variables (time, latitude and longitude) as proxy variables and the second column (b, e) shows those with coordinate proxies. The last column (c, f) shows estimates trained with random locations (uniform in time and space) with coordinate proxies. The metrics are shown on each plot where MAE and RMSE are mean absolute error and root mean squared error, respectively. The number of observations in the estimate is denoted by  $n$ .



*Competing interests.* The authors declare that they have no conflict of interest.

*Acknowledgements.* This work is part of a PhD funded by the ACCESS program. The authors would like to thank Marina Lévy for use of the BIOPERIANT05-GAA95b model data. This work was partly enabled by the Centre for High Performance Computing (CSIR).

The Surface Ocean CO<sub>2</sub> Atlas (SOCAT) is an international effort, endorsed by the International Ocean Carbon Coordination Project (IOCCP), the Surface Ocean Lower Atmosphere Study (SOLAS) and the Integrated Marine Biogeochemistry and Ecosystem Research program (IMBER), to deliver a uniformly quality-controlled surface ocean CO<sub>2</sub> database. The many researchers and funding agencies responsible for the collection of data and quality control are thanked for their contributions to SOCAT.

Edited by: Laurent Bopp

Reviewed by: Nicolas Gruber and one anonymous referee

## References

- Atlas, R., Hoffman, R. N., Ardizzone, J., Leidner, S. M., Jusem, J. C., Smith, D. K., and Gombos, D.: A Cross-calibrated, Multi-platform Ocean Surface Wind Velocity Product for Meteorological and Oceanographic Applications, *B. Am. Meteorol. Soc.*, 92, 157–174, <https://doi.org/10.1175/2010BAMS2946.1>, 2011.
- Bakker, D. C. E., Hoppema, M., Schröder, M., Geibert, W., and de Baar, H. J. W.: A rapid transition from ice covered CO<sub>2</sub>-rich waters to a biologically mediated CO<sub>2</sub> sink in the eastern Weddell Gyre, *Biogeosciences*, 5, 1373–1386, <https://doi.org/10.5194/bg-5-1373-2008>, 2008.
- Bakker, D. C. E., Pfeil, B., Landa, C. S., Metzl, N., O'Brien, K. M., Olsen, A., Smith, K., Cosca, C., Harasawa, S., Jones, S. D., Nakaoka, S.-I., Nojiri, Y., Schuster, U., Steinhoff, T., Sweeney, C., Takahashi, T., Tilbrook, B., Wada, C., Wanninkhof, R., Alin, S. R., Balestrini, C. F., Barbero, L., Bates, N. R., Bianchi, A. A., Bonou, F., Boutin, J., Bozec, Y., Burger, E. F., Cai, W.-J., Castle, R. D., Chen, L., Chierici, M., Currie, K., Evans, W., Featherstone, C., Feely, R. A., Fransson, A., Goyet, C., Greenwood, N., Gregor, L., Hankin, S., Hardman-Mountford, N. J., Harlay, J., Hauck, J., Hoppema, M., Humphreys, M. P., Hunt, C. W., Huss, B., Ibáñez, J. S. P., Johannessen, T., Keeling, R., Kitidis, V., Körtzinger, A., Kozyr, A., Krasakopoulou, E., Kuwata, A., Landschützer, P., Lauvset, S. K., Lefèvre, N., Lo Monaco, C., Manke, A., Mathis, J. T., Merlivat, L., Millero, F. J., Monteiro, P. M. S., Munro, D. R., Murata, A., Newberger, T., Omar, A. M., Ono, T., Paterson, K., Pearce, D., Pierrot, D., Robbins, L. L., Saito, S., Salisbury, J., Schlitzer, R., Schneider, B., Schweitzer, R., Sieger, R., Skjelvan, I., Sullivan, K. F., Sutherland, S. C., Sutton, A. J., Tadokoro, K., Telszewski, M., Tuma, M., van Heuven, S. M. A. C., Vandemark, D., Ward, B., Watson, A. J., and Xu, S.: A multi-decade record of high-quality *f*CO<sub>2</sub> data in version 3 of the Surface Ocean CO<sub>2</sub> Atlas (SOCAT), *Earth Syst. Sci. Data*, 8, 383–413, <https://doi.org/10.5194/essd-8-383-2016>, 2016.
- Biastoch, A., Böning, C. W., Getzlaff, J., Molines, J.-M., and Madec, G.: Causes of Interannual–Decadal Variability in the Meridional Overturning Circulation of the Mid-latitude North Atlantic Ocean, *J. Climate*, 21, 6599–6615, <https://doi.org/10.1175/2008JCLI2404.1>, 2008.
- Boyd, P. W. and Ellwood, M. J.: The biogeochemical cycle of iron in the ocean, *Nat. Geosci.*, 3, 675–682, <https://doi.org/10.1038/ngeo964>, 2010.
- Breiman, L.: Random forests, *Mach. Learn.*, 45, 5–32, <https://doi.org/10.1023/A:1010933404324>, 2001.
- Carranza, M. M. and Gille, S. T.: Southern Ocean wind-driven entrainment enhances satellite chlorophyll-a through the summer, *J. Geophys. Res.-Oceans*, 120, 304–323, <https://doi.org/10.1002/2014JC010203>, 2015.
- Caruana, R. and Niculescu-Mizil, A.: An empirical comparison of supervised learning algorithms, *Proceedings of the 23th International Conference on Machine Learning*, pp. 161–168, <https://doi.org/10.1145/1143844.1143865>, 2006.
- Chierici, M., Signorini, S. R., Mattsdotter-Björk, M., Fransson, A., and Olsen, A.: Surface water fCO<sub>2</sub> algorithms for the high-latitude Pacific sector of the Southern Ocean, *Remote Sens. Environ.*, 119, 184–196, <https://doi.org/10.1016/j.rse.2011.12.020>, 2012.
- Dufour, C. O., Sommer, L. L., Zika, J. D., Gehlen, M., Orr, J. C., Mathiot, P., and Barnier, B.: Standing and transient eddies in the response of the Southern Ocean meridional overturning to the Southern annular mode, *J. Climate*, 25, 6958–6974, <https://doi.org/10.1175/JCLI-D-11-00309.1>, 2012.
- Fay, A. R. and McKinley, G. A.: Global open-ocean biomes: mean and temporal variability, *Earth Syst. Sci. Data*, 6, 273–284, <https://doi.org/10.5194/essd-6-273-2014>, 2014.
- Friedrich, T. and Oschlies, A.: Neural network-based estimates of North Atlantic surface pCO<sub>2</sub> from satellite data: A methodological study, *J. Geophys. Res.*, 114, 1–12, <https://doi.org/10.1029/2007JC004646>, 2009.
- Frölicher, T. L., Sarmiento, J. L., Paynter, D. J., Dunne, J. P., Krasting, J. P., and Winton, M.: Dominance of the Southern Ocean in anthropogenic carbon and heat uptake in CMIP5 models, *J. Climate*, 28, 862–886, <https://doi.org/10.1175/JCLI-D-14-00117.1>, 2015.
- Gade, K.: A Non-singular Horizontal Position Representation, *J. Navigation*, 63, 395–417, <https://doi.org/10.1017/S0373463309990415>, 2010.
- Gregor, L., Kok, S., and Monteiro, P. M. S.: Dataset for empirically estimated pCO<sub>2</sub> for the Southern Ocean: RFR and SVR, <https://doi.org/10.6084/m9.figshare.5369038>, 2017.
- Hastie, T., Tibshirani, R., and Friedman, J.: *The Elements of Statistical Learning: Data mining, Inference, and Prediction*, Springer, 2nd Edn., 2009.
- Hoyer, S. and Hamman, J. J.: xarray: N-D labeled Arrays and Datasets in Python, *Journal of Open Research Software*, 5, 1–6, <https://doi.org/10.5334/jors.148>, 2017.
- Johnson, K. S., Plant, J. N., Coletti, L. J., Jannasch, H. W., Sakamoto, C. M., Riser, S. C., Swift, D. D., Williams, N. L., Boss, E., Haëntjens, N., Talley, L. D., and Sarmiento, J. L.: Biogeochemical sensor performance in the SOCCOM profiling float array, *J. Geophys. Res.-Oceans*, 122, 6416–6436, <https://doi.org/10.1002/2017JC012838>, 2017.

- Jones, S. D., Le Quéré, C., and Rdenbeck, C.: Autocorrelation characteristics of surface ocean pCO<sub>2</sub> and air-sea CO<sub>2</sub> fluxes, *Global Biogeochem. Cy.*, 26, 1–12, <https://doi.org/10.1029/2010GB004017>, 2012.
- Kanamitsu, M., Ebisuzaki, W., Woollen, J., Yang, S. K., Hnilo, J. J., Fiorino, M., and Potter, G. L.: NCEP-DOE AMIP-II reanalysis (R-2), *B. Am. Meteorol. Soc.*, 83, 1631–1643+1559, <https://doi.org/10.1175/BAMS-83-11-1631>, 2002.
- Khatiwalala, S., Tanhua, T., Mikaloff Fletcher, S., Gerber, M., Doney, S. C., Graven, H. D., Gruber, N., McKinley, G. A., Murata, A., Ríos, A. F., and Sabine, C. L.: Global ocean storage of anthropogenic carbon, *Biogeosciences*, 10, 2169–2191, <https://doi.org/10.5194/bg-10-2169-2013>, 2013.
- Landschützer, P., Gruber, N., Bakker, D. C., and Schuster, U.: Recent variability of the global ocean carbon sink, *Global Planet. Change*, 927–949, <https://doi.org/10.1002/2014GB004853>, 2014.
- Landschützer, P., Gruber, N., Haumann, F. A., Rödenbeck, C., Bakker, D. C., Van Heuven, S. M., Hoppema, M., Metzl, N., Sweeney, C., Takahashi, T. T., Tilbrook, B., and Wanninkhof, R. H.: The reinvigoration of the Southern Ocean carbon sink, *Science*, 349, 1221–1224, <https://doi.org/10.1126/science.aab2620>, 2015.
- Lenton, A., Matear, R. J., and Tilbrook, B.: Design of an observational strategy for quantifying the Southern Ocean uptake of CO<sub>2</sub>, *Global Biogeochem. Cy.*, 20, GB4010, <https://doi.org/10.1029/2005GB002620>, 2006.
- Lenton, A., Metzl, N., Takahashi, T. T., Kuchinke, M., Matear, R. J., Roy, T., Sutherland, S. C., Sweeney, C., and Tilbrook, B.: The observed evolution of oceanic pCO<sub>2</sub> and its drivers over the last two decades, *Global Biogeochem. Cy.*, 26, 1–14, <https://doi.org/10.1029/2011GB004095>, 2012.
- Lenton, A., Tilbrook, B., Law, R. M., Bakker, D., Doney, S. C., Gruber, N., Ishii, M., Hoppema, M., Lovenduski, N. S., Matear, R. J., McNeil, B. I., Metzl, N., Mikaloff Fletcher, S. E., Monteiro, P. M. S., Rödenbeck, C., Sweeney, C., and Takahashi, T.: Sea-air CO<sub>2</sub> fluxes in the Southern Ocean for the period 1990–2009, *Biogeosciences*, 10, 4037–4054, <https://doi.org/10.5194/bg-10-4037-2013>, 2013.
- Le Quéré, C., Rödenbeck, C., Buitenhuis, E. T., Conway, T. J., Langenfelds, R., Gomez, A., Labuschagne, C., Ramonet, M., Nakazawa, T., Metzl, N., Gillett, N. P., and Heimann, M.: Saturation of the Southern Ocean CO<sub>2</sub> Sink Due to Recent Climate Change, *Science*, 316, 1735–1738, <https://doi.org/10.1126/science.1137004>, 2007.
- Le Quéré, C., Andrew, R. M., Canadell, J. G., Sitch, S., Korsbakken, J. I., Peters, G. P., Manning, A. C., Boden, T. A., Tans, P. P., Houghton, R. A., Keeling, R. F., Alin, S., Andrews, O. D., Anthoni, P., Barbero, L., Bopp, L., Chevallier, F., Chini, L. P., Ciais, P., Currie, K., Delire, C., Doney, S. C., Friedlingstein, P., Gkritzalis, T., Harris, I., Hauck, J., Haverd, V., Hoppema, M., Klein Goldewijk, K., Jain, A. K., Kato, E., Körtzinger, A., Landschützer, P., Lefèvre, N., Lenton, A., Lienert, S., Lombardozi, D., Melton, J. R., Metzl, N., Millero, F., Monteiro, P. M. S., Munro, D. R., Nabel, J. E. M. S., Nakaoka, S.-I., O'Brien, K., Olsen, A., Omar, A. M., Ono, T., Pierrot, D., Poulter, B., Rödenbeck, C., Salisbury, J., Schuster, U., Schwinger, J., Séférian, R., Skjelvan, I., Stocker, B. D., Sutton, A. J., Takahashi, T., Tian, H., Tilbrook, B., van der Laan-Luijkx, I. T., van der Werf, G. R., Viovy, N., Walker, A. P., Wiltshire, A. J., and Zaehle, S.: Global Carbon Budget 2016, *Earth Syst. Sci. Data*, 8, 605–649, <https://doi.org/10.5194/essd-8-605-2016>, 2016.
- Loh, W.-Y.: Classification and regression trees, *Wires Data Min. Knowl.*, 1, 14–23, <https://doi.org/10.1002/widm.8>, 2011.
- Louppe, G.: Understanding random forests: from theory to practice, PhD thesis, University of Liege, 2014.
- Maritorena, S. and Siegel, D. A.: Consistent merging of satellite ocean color data sets using a bio-optical model, *Remote Sens. Environ.*, 94, 429–440, <https://doi.org/10.1016/j.rse.2004.08.014>, 2005.
- Masarie, K. A., Peters, W., Jacobson, A. R., and Tans, P. P.: ObsPack: a framework for the preparation, delivery, and attribution of atmospheric greenhouse gas measurements, *Earth Syst. Sci. Data*, 6, 375–384, <https://doi.org/10.5194/essd-6-375-2014>, 2014.
- Menemenlis, D., Campin, J.-M., Heimbach, P., Hill, C. N., Lee, T., Nguyen, A., Schodlok, M., and Zhang, H.: ECCO2: High Resolution Global Ocean and Sea Ice Data Synthesis, *Mercator Ocean Quarterly Newsletter*, 31, 13–21, 2008.
- Met Office: Iris: A Python library for analysing and visualising meteorological and oceanographic data sets, Exeter, Devon, v1.2 Edn., available at: <http://scitools.org.uk/>, last access: 12 August 2017.
- Metzl, N., Brunet, C., Jabaud-Jan, A., Poisson, A., and Schauer, B.: Summer and winter air-sea CO<sub>2</sub> fluxes in the Southern Ocean, *Deep-Sea Res. Pt. I*, 53, 1548–1563, <https://doi.org/10.1016/j.dsr.2006.07.006>, 2006.
- Mongwe, N. P., Chang, N., and Monteiro, P. M. S.: The seasonal cycle as a mode to diagnose biases in modelled CO<sub>2</sub> fluxes in the Southern Ocean, *Ocean Model.*, 106, 90–103, <https://doi.org/10.1016/j.ocemod.2016.09.006>, 2016.
- Monteiro, P. M. S.: A Global Sea Surface Carbon Observing System: Assessment of Changing Sea Surface CO<sub>2</sub> and Air-Sea CO<sub>2</sub> Fluxes, *Proceedings of OceanObs'09: Sustained Ocean Observations and Information for Society*, 702–714, <https://doi.org/10.5270/OceanObs09.cwp.64>, 2010.
- Mountrakis, G., Im, J., and Ogole, C.: Support vector machines in remote sensing: A review, *ISPRS J. Photogramme.g.*, 66, 247–259, <https://doi.org/10.1016/j.isprsjprs.2010.11.001>, 2011.
- Pedregosa, F., Varoquaux, G., Gramfort, A., Michel, C., Thirion, B., Grisel, O., Blondel, M., Prettenhoffer, P., Weiss, R., Dubourg, V., Vanderplas, J., Passos, A., and Cournapeau, D.: Scikit-learn: Machine learning in Python, *J. Mach. Learn. Res.*, 12, 2825–2830, 2011.
- Reynolds, R. W., Smith, T. M., Liu, C., Chelton, D. B., Casey, K. S., and Schlax, M. G.: Daily high-resolution-blended analyses for sea surface temperature, *J. Climate*, 20, 5473–5496, <https://doi.org/10.1175/2007JCLI1824.1>, 2007.
- Rödenbeck, C., Bakker, D. C. E., Metzl, N., Olsen, A., Sabine, C., Cassar, N., Reum, F., Keeling, R. F., and Heimann, M.: Interannual sea-air CO<sub>2</sub> flux variability from an observation-driven ocean mixed-layer scheme, *Biogeosciences*, 11, 4599–4613, <https://doi.org/10.5194/bg-11-4599-2014>, 2014.
- Rödenbeck, C., Bakker, D. C. E., Gruber, N., Iida, Y., Jacobson, A. R., Jones, S., Landschützer, P., Metzl, N., Nakaoka, S., Olsen, A., Park, G.-H., Peylin, P., Rodgers, K. B., Sasse, T. P., Schuster, U., Shutler, J. D., Valsala, V., Wanninkhof, R., and Zeng, J.: Data-based estimates of the ocean carbon sink

- variability – first results of the Surface Ocean pCO<sub>2</sub> Mapping intercomparison (SOCOM), *Biogeosciences*, 12, 7251–7278, <https://doi.org/10.5194/bg-12-7251-2015>, 2015.
- Russell, J. L., Sarmiento, J. L., Cullen, H., Hotinski, R., Johnson, K. S., Riser, S. C., and Talley, L. D.: The Southern Ocean Carbon and Climate Observations and Modeling Program (SOCCOM), *Ocean Carbon and Biogeochemistry Article*, 7, 1–28, 2014.
- Sasse, T. P., McNeil, B. I., and Abramowitz, G.: A novel method for diagnosing seasonal to inter-annual surface ocean carbon dynamics from bottle data using neural networks, *Biogeosciences*, 10, 4319–4340, <https://doi.org/10.5194/bg-10-4319-2013>, 2013.
- Smola, A. J., Schölkopf, B., and Olkorf, B.: A Tutorial on Support Vector Regression, *Stat. Comput.*, 14, 199–222, <https://doi.org/10.1023/B:Stco.0000035301.49549.88>, 2004.
- Tagliabue, A., Sallée, J.-B., Bowie, A. R., Lévy, M., Swart, S., and Boyd, P. W.: Surface-water iron supplies in the Southern Ocean sustained by deep winter mixing, *Nat. Geosci.*, 7, 314–320, <https://doi.org/10.1038/NNGEO2101>, 2014.
- Takahashi, T. T., Sutherland, S. C., Sweeney, C., Poisson, A., Metzl, N., Tilbrook, B., Bates, N. R., Wanninkhof, R. H., Feely, R. A., Sabine, C. L., Olafsson, J., and Nojiri, Y.: Global sea-air CO<sub>2</sub> flux based on climatological surface ocean pCO<sub>2</sub>, and seasonal biological and temperature effects, *Deep-Sea Res. Pt. II*, 49, 1601–1622, [https://doi.org/10.1016/S0967-0645\(02\)00003-6](https://doi.org/10.1016/S0967-0645(02)00003-6), 2002.
- Takahashi, T. T., Sweeney, C., Hales, B., Chipman, D. W., Newberger, T., Goddard, J. G., Iannuzzi, R., and Sutherland, S. C.: The Changing Carbon Cycle in the Southern Ocean, *Oceanography*, 25, 26–37, <https://doi.org/10.5670/oceanog.2012.71>, 2012.
- Thomalla, S. J., Fauchereau, N., Swart, S., and Monteiro, P. M. S.: Regional scale characteristics of the seasonal cycle of chlorophyll in the Southern Ocean, *Biogeosciences*, 8, 2849–2866, <https://doi.org/10.5194/bg-8-2849-2011>, 2011.
- Vapnik, V.: An overview of statistical learning theory, *IEEE T. Neural Netw.*, 10, 988–999, <https://doi.org/10.1109/72.788640>, 1999.
- Wanninkhof, R. H.: Relationship between wind speed and gas exchange over the ocean revisited, *Limnol. Oceanogr.*, 12, 351–362, <https://doi.org/10.4319/lom.2014.12.351>, 2014.
- Weiss, R.: Carbon dioxide in water and seawater: the solubility of a non-ideal gas, *Mar. Chem.*, 2, 203–215, [https://doi.org/10.1016/0304-4203\(74\)90015-2](https://doi.org/10.1016/0304-4203(74)90015-2), 1974.
- Williams, N. L., Juraneck, L. W., Feely, R. A., Johnson, K. S., Sarmiento, J. L., Talley, L. D., Dickson, A. G., Gray, A. R., Wanninkhof, R. H., Russell, J. L., Riser, S. C., and Takeshita, Y.: Calculating surface ocean pCO<sub>2</sub> from biogeochemical Argo floats equipped with pH: An uncertainty analysis, *Global Biogeochem. Cy.*, 31, 591–604, <https://doi.org/10.1002/2016GB005541>, 2017.